

## THE DYNAMICAL MASSES, DENSITIES, AND STAR FORMATION SCALING RELATIONS OF Ly $\alpha$ GALAXIES

JAMES E. RHOADS<sup>1</sup>, SANGEETA MALHOTRA<sup>1</sup>, MARK L. A. RICHARDSON<sup>1</sup>, STEVEN L. FINKELSTEIN<sup>2</sup>,  
JOHAN P. U. FYNBO<sup>3</sup>, EMILY M. MCLINDEN<sup>1,2</sup>, AND VITHAL S. TILVI<sup>4</sup>

<sup>1</sup> School of Earth and Space Exploration, Arizona State University, Tempe, AZ 85287, USA; James.Rhoads@asu.edu

<sup>2</sup> Department of Astronomy, University of Texas at Austin, 1 University Station C1400, Austin, TX 78712, USA

<sup>3</sup> DARK Cosmology Centre, Niels Bohr Institute, University of Copenhagen, Juliane Maries Vej 30, DK-2100 Copenhagen Ø, Denmark

<sup>4</sup> George P. and Cynthia W. Mitchell Institute for Fundamental Physics and Astronomy, Department of Physics,  
Texas A&M University, College Station, TX 77843, USA

Received 2012 December 30; accepted 2013 August 23; published 2013 December 10

### ABSTRACT

We present the first dynamical mass measurements for Ly $\alpha$  galaxies at high redshift, based on velocity dispersion measurements from rest-frame optical emission lines and size measurements from *Hubble Space Telescope* imaging, for nine galaxies drawn from four surveys. We use these measurements to study Ly $\alpha$  galaxies in the context of galaxy scaling relations. The resulting dynamical masses range from  $10^9$  to  $10^{10} M_{\odot}$ . We also fit stellar population models to our sample and use them to place the Ly $\alpha$  sample on a stellar mass versus line width relation. The Ly $\alpha$  galaxies generally follow the same scaling relation as star-forming galaxies at lower redshift, although, lower stellar mass fits are also acceptable in  $\sim 1/3$  of the Ly $\alpha$  galaxies. Using the dynamical masses as an upper limit on gas mass, we show that Ly $\alpha$  galaxies have unusually active star formation for their gas mass surface density. This behavior is consistent with what is observed in starburst galaxies, despite the typically smaller masses and sizes of the Ly $\alpha$  galaxy population. Finally, we examine the mass densities of these galaxies and show that their future evolution likely requires dissipational (“wet”) merging. In short, we find that Ly $\alpha$  galaxies are low-mass cousins of larger starbursts.

*Key words:* galaxies: evolution – galaxies: formation – galaxies: high-redshift

*Online-only material:* color figures

### 1. INTRODUCTION

Ly $\alpha$  line emission is an increasingly important tool for identifying actively star-forming galaxies in the distant universe. Ly $\alpha$  emission was proposed as a potential signpost for primitive galaxies (Partridge & Peebles 1967) and has now been used to identify thousands of galaxies at redshifts  $2 < z < 7$ , along with smaller samples at  $z < 2$  and several candidates at  $z > 7$ .

While no galaxy yet identified by any means is demonstrably primordial, Ly $\alpha$ -selected samples do have several properties suggestive of youth. Their starlight is dominated by young populations with characteristically low stellar masses (Pirzkal et al. 2007; Finkelstein et al. 2007) and small sizes (Bond et al. 2009; Malhotra et al. 2012). Yet, the correlation properties of these objects suggest that they are associated with moderately large halos (mass  $\sim 10^{11} M_{\odot}$ ; Kovač et al. 2007; Guaita et al. 2010). Combining these results suggests that a Ly $\alpha$  galaxy contains only a small fraction of the baryons that should be associated with its host dark matter halo. It would be interesting to know whether the “missing” baryons are present, either as old stellar populations or in the interstellar medium of the Ly $\alpha$  galaxy.

Dynamical mass estimates for Ly $\alpha$  galaxies could potentially address this question. The dynamical mass is the total gravitating mass of the galaxy, measured using kinematics. Such masses provide a standard for comparison with both the stellar masses and the dark halo masses. However, dynamical mass estimates require an accurate measurement of the galaxy’s velocity dispersion. The easiest approach to kinematics would be to use the Ly $\alpha$  line width, which is measured for most spectroscopically confirmed Ly $\alpha$  galaxies. Unfortunately, this does not lead to useful velocity dispersion information as the Ly $\alpha$  line profile can

be dramatically affected by the interplay of resonant scattering and gas kinematics in the emitting galaxy.

We therefore turn in this paper to studying Ly $\alpha$  galaxy kinematics using the strong rest-frame optical emission lines of [O III]  $\lambda 5007$  Å and H $\alpha$   $\lambda 6561$  Å. We build on the first detections of such lines in Ly $\alpha$ -selected galaxies at redshifts  $2.2 \lesssim z \lesssim 3.1$  (McLinden et al. 2011; Finkelstein et al. 2011; Hashimoto et al. 2012). In Section 2, we describe the sample and the key data. In Section 3, we estimate dynamical masses based on the observed line widths. In Section 4, we analyze the stellar populations and dust reddening in these galaxies, using deep archival photometry. In Section 5, we combine the rest-optical line width measurements with the stellar masses from population synthesis modeling to compare these Ly $\alpha$  galaxies with expectations from the stellar mass Tully–Fisher (SMTF) relation (e.g., Kassin et al. 2007). In Section 6, we examine the relation between gas mass surface density and star formation surface density to show that Ly $\alpha$  galaxies lie on the same sequence as starburst galaxies. Finally, in Section 7, we explore the mass densities of the sample and the implications for the future evolution of Ly $\alpha$  galaxies.

Throughout the paper, we adopt a  $\Lambda$ -CDM “concordance cosmology” with  $\Omega_M = 0.27$ ,  $\Omega_{\Lambda} = 0.73$ , and  $H_0 = 71 \text{ km s}^{-1} \text{ Mpc}^{-1}$ .

### 2. DESCRIPTION OF THE SAMPLE

Our sample consists of Ly $\alpha$  emitting galaxies that were selected from four surveys. All are selected directly by the presence of a strong Ly $\alpha$  emission line in the survey data. For the analysis in this paper, we make use of (1) velocity dispersions  $\sigma$ , derived from spectra of rest-frame optical emission lines,

**Table 1**  
Basic Observational Properties of the Sample

ID	$z$	$\sigma_{\text{los}}$	$d(\sigma_{\text{los}})$	$r_e$ (kpc)	SFR	$d(\text{SFR})$	Refs. <sup>a</sup>
LAE40845	3.1117	81	+4 -4	1.1	113 <sup>b</sup>	+120 -60	1
LAE27878	3.11879	43	+7 -7	1.3	32 <sup>b</sup>	+9 -7	1
HPS194	2.287	65	+6 -6	1.5	17	+1.5 -0.5	2
HPS256	2.491	74	+7 -8	1.1	25	+9 -5	2
COSMOS13636	2.1621	57	+40 -57	0.79	7.4	+2.5 -2	3
COSMOS30679	2.19855	55	+40 -55	1.83	31	+38 -15	3
CDFS3865	2.173	105	+20 -20	0.96	96	+21 -15	3
CDFS6482	2.205	42	+28 -42	1.78	29	+10 -7	3
LAE-COSMOS-47	2.24654	27	+7 -8	1.14	16.3	+4.6 -1.0	4

#### Notes.

<sup>a</sup> References: 1. McLinden et al. 2011; Richardson et al. 2013; 2. Finkelstein et al. 2011; Song et al. 2013; 3. Hashimoto et al. 2012; Nakajima et al. 2012; 4. Nilsson et al. 2011.

<sup>b</sup> SFR is based on SED fitting results for this object.

(2) sizes, as measured by the half-light radius  $r_e$  in broadband optical *Hubble Space Telescope* (*HST*) images, (3) stellar masses and dust extinctions, derived from spectral energy distribution (SED) fits, and (4) star formation rates (SFRs), determined from  $\text{H}\alpha$  line flux measurements, where available ( $\text{SFR}_{\text{H}\alpha}$ ), and from SED fitting otherwise ( $\text{SFR}_{\text{sed}}$ ), and corrected for dust obscuration using the results of the SED fits. In this section, we summarize the sources for various galaxies in the sample, along with the measurements of  $\sigma$ ,  $r_e$ , and SFR. The stellar mass derivations are discussed later, in Section 4.

The properties of the sample are also tabulated. Basic observational quantities ( $z$ ,  $\sigma_{\text{los}}$ ,  $r_e$ ) and derived SFRs are in Table 1. Dynamical masses and densities are in Table 2, along with the range of stellar masses from SED fitting. More detailed SED fitting results are summarized in Tables 3 and 4.

### 2.1. Bok Telescope $z = 3.1$ Survey Objects

First, we select two  $\text{Ly}\alpha$  galaxies from a 5020 Å narrow-band survey using the Steward Observatory’s 90 inch Bok Telescope on Kitt Peak, Arizona. The objects we study here were spectroscopically confirmed as  $\text{Ly}\alpha$  emitters at  $z \approx 3.12$  using the 6.5 m MMT on Mt. Hopkins, Arizona. This survey was introduced in McLinden et al. (2011) and further details will be presented in a forthcoming paper (McLinden et al. 2013). We have followed up galaxies from this sample with three near-infrared spectrographs: LUCIFER, on the Large Binocular Telescope (McLinden et al. 2011), NIFS, on Gemini North (Richardson et al. 2013), and NIRSPEC, on the Keck II telescope (McLinden et al. 2013). The objects studied here are LAE40844 and LAE27878 (following the numbering in McLinden et al. 2011); we hereafter refer to these objects as 40844 and 27878, respectively.

The primary source of line widths for these objects is our Gemini NIFS data (Richardson et al. 2013), since our Keck observations of 40844 were primarily aimed at the (still undetected)  $[\text{O III}] \lambda\lambda 3726, 3729$  lines, while the kinematic line width is not well resolved in the LUCIFER observations. Richardson et al. (2013) fit the observed lines in the extracted one-dimensional spectra with Gaussian profiles and determined the uncertainties by adding simulated noise to the data and refitting (many times). This procedure yielded line widths of  $\Delta\lambda_{\text{FWHM}}([\text{O III}]5007) = 13.8 \pm 0.6 \text{ \AA}$  for object 40844 and

**Table 2**  
Masses and Densities of the Sample

ID	$M_{\text{dyn}}^a$	$\log(\bar{\rho}_e)^b$	$M_{s,\text{min}}^a$	$M_{s,\text{max}}^a$		
LAE40844	6.7	+0.6 -0.6	-22.39	+0.10 -0.10	2.72	34.0
LAE27878	2.2	+0.8 -0.8	-23.08	+0.35 -0.35	3.80	22.5
HPS194	5.8	+1.3 -1.3	-22.85	+0.27 -0.27	19.9	21.2
HPS256	5.6	+1.4 -1.4	-22.47	+0.30 -0.30	1.75	11.3
COSMOS13636	2.4	+5.1 -2.4	-22.40	+1.2 -∞	4.22	11.0
COSMOS30679	5.1	+11 -5.1	-23.16	+1.2 -∞	1.65	12.0
CDFS3865	9.8	+5.6 -4.3	-22.04	+0.45 -0.58	6.52	14.3
CDFS6482	2.9	+3.3 -2.9	-23.38	+0.76 -∞	9.10	32.7
LAE-COSMOS-47	0.95	+0.77 -0.55	-23.28	+0.75 -0.98	0.5768	2.13

**Notes.** The dynamically derived masses, the dynamically derived mean volume mass densities inside the effective radius, and the  $1\sigma$  range of stellar masses derived from SED fitting.

<sup>a</sup> All masses are given in units of  $10^9 M_{\odot}$ .

<sup>b</sup> Densities are given in units of  $\text{g cm}^{-3}$ .

$8.6 \pm 0.9 \text{ \AA}$  for object 27878. The instrumental resolution was about 5 Å. Subtracting this instrumental resolution in quadrature from the measured line widths yields 13.0 Å and 7.0 Å, respectively. The corresponding line-of-sight velocity dispersions become  $\sigma_{\text{los}} = 81 \pm 4 \text{ km s}^{-1}$  and  $\sigma_{\text{los}} = 43 \pm 7 \text{ km s}^{-1}$ , respectively.

The half-light radii for these objects are 1.1 kpc for 40844 and 1.3 kpc for 27878. These are based on the COSMOS Advanced Camera for Surveys (ACS) *i*-band catalog (Leauthaud et al. 2007), as cited in Malhotra et al. (2012). We estimated their  $\text{SFR}_{\text{sed}}$  values from SED fitting (Section 4), since their  $\text{H}\alpha$  line falls at  $2.70 \mu\text{m}$  and cannot be easily observed. We obtained  $113 M_{\odot} \text{ yr}^{-1}$  for 40844 and  $32 M_{\odot} \text{ yr}^{-1}$  for 27878. We estimate the uncertainties in these SFRs from the range of  $\text{SFR}_{\text{sed}}$  values in models that yielded acceptable fits to the data (see Section 4).

### 2.2. HETDEX Pilot Survey Objects

Second, we use two  $\text{Ly}\alpha$  galaxies selected using a blind spectroscopic search with an integral field spectrograph as part of the HETDEX Pilot Survey. These are objects HPS194 ( $z = 2.287$ ) and HPS256 ( $z = 2.491$ ). For these, we base our kinematic line widths on Keck+NIRSPEC  $\text{H}\alpha$  line measurements from Finkelstein et al. (2011) and Song et al. (2013). These used the low-resolution mode with the NSPEC-7 blocking filter. The measured line widths were  $\Delta\lambda_{\text{FWHM}}(\text{H}\alpha) = 18.1 \pm 0.6 \text{ \AA}$  for HPS194 and  $\Delta\lambda_{\text{FWHM}}(\text{H}\alpha) = 19.4 \pm 0.9 \text{ \AA}$  for HPS256. The instrumental resolving power is  $R \sim 1500$  with the 0.76 slit, corresponding to 14–15 Å FWHM, and direct measurements of sky lines in the two spectra yield resolutions of 14.4 Å and 14.1 Å (FWHM), respectively. Subtracting these in quadrature yields line widths of 11.0 Å and 13.3 Å, respectively. The corresponding line-of-sight velocity dispersions become  $\sigma_{\text{los}} = 65 \pm 6 \text{ km s}^{-1}$  and  $\sigma_{\text{los}} = 74_{-8}^{+7} \text{ km s}^{-1}$ , respectively. The half-light radii, as reported in the COSMOS ACS *i*-band catalog (Leauthaud et al. 2007), are 1.5 kpc for HPS194 and 1.1 kpc for HPS256. (HPS194 in fact corresponds to a pair of continuum sources separated by  $\sim 0.5$  in the COSMOS survey’s *HST*+ACS images. We assume that the strong  $\text{Ly}\alpha$  and  $\text{H}\alpha$  emission come from the brighter and more compact source. The other source has a 2.4 kpc half-light radius, which would raise our dynamical mass for this object by about 60%.)

**Table 3**  
Best-fitting SED Model for Each Object

ID	Age 1 <sup>a</sup>	Mass 1 <sup>b</sup>	Age 2 <sup>a</sup>	Mass 2 <sup>b</sup>	Age 3 <sup>a</sup>	Mass 3 <sup>b</sup>	$M_{\text{tot}}$	$A_B$	$\chi^2$	$N_{\text{bands}}^c$
LAE40844	2	$2.61 \times 10^8$	8	$5.20 \times 10^8$	300	$5.48 \times 10^9$	$6.27 \times 10^9$	0.217	42.227	11
LAE27878	2	$6.54 \times 10^7$	600	$9.36 \times 10^9$	0	0	$9.43 \times 10^9$	0.164	3.269	11
HPS194	2	$5.19 \times 10^7$	300	$2.05 \times 10^{10}$	0	0	$20.54 \times 10^9$	0	14.92	9
HPS256	2	$3.59 \times 10^7$	1500	$3.58 \times 10^9$	0	0	$3.61 \times 10^9$	0.111	2.656	9
COSMOS13636	4	$9.95 \times 10^7$	300	$8.02 \times 10^9$	0	0	$8.12 \times 10^9$	0.258	35.15	9
COSMOS30679	4	$9.40 \times 10^8$	150	$3.72 \times 10^9$	0	0	$4.66 \times 10^9$	0.906	20.22	9
CDFS3865	2	$3.04 \times 10^8$	150	$7.41 \times 10^9$	0	0	$7.71 \times 10^9$	0.211	7.672	12
CDFS6482	2	$1.35 \times 10^8$	16	$5.86 \times 10^8$	2000	$2.11 \times 10^{10}$	$21.9 \times 10^9$	0.299	3.862	11
LAE-COSMOS-47	4	$2.47 \times 10^7$	300	$9.71 \times 10^8$	0	0	$0.996 \times 10^9$	0	27.5	19

**Notes.** For each galaxy studied, we report the single best-fitting stellar population model that we found. Each model consists of up to three single-age bursts of star formation. The ages and masses for these bursts are given in Columns 2–7 and the total mass of all bursts is given in Column 8. All the modeled stars are obscured by a single common dust screen with  $B$ -band extinction  $A_B$  (Column 9). In addition to these model parameters, we report the  $\chi^2$  value of the model (Column 10) and the number of photometric bands used in the SED fitting (column 11).

<sup>a</sup> Ages in Myr.

<sup>b</sup> Masses in  $M_{\odot}$ .

<sup>c</sup> Number of photometric bands used in SED fitting. Wavelength coverage always extends at least from the  $B$  band ( $0.44 \mu\text{m}$ ) to IRAC Channel 1 ( $3.6 \mu\text{m}$ ).

**Table 4**  
Range of SED Fitting Results for the Sample

ID	$M_{-2\sigma}$	$M_{*, -1\sigma}$	$M_{*, +1\sigma}$	$M_{*, +2\sigma}$	$A_{B, -2\sigma}$	$A_{B, -1\sigma}$	$A_{B, \text{best}}$	$A_{B, +1\sigma}$	$A_{B, +2\sigma}$
LAE40844	$9.43 \times 10^8$	$2.72 \times 10^9$	$3.40 \times 10^{10}$	$3.91 \times 10^{10}$	0.081	0.150	0.217	0.22	0.241
LAE27878	$1.66 \times 10^9$	$3.80 \times 10^9$	$2.25 \times 10^{10}$	$3.62 \times 10^{10}$	0	0	0.164	0.201	0.254
HPS194	$1.93 \times 10^{10}$	$1.99 \times 10^{10}$	$2.12 \times 10^{10}$	$2.30 \times 10^{10}$	0	0	0	0.030	0.100
HPS256	$9.64 \times 10^7$	$1.75 \times 10^9$	$1.13 \times 10^{10}$	$2.03 \times 10^{10}$	0	0.009	0.110	0.199	0.298
COSMOS13636	$2.45 \times 10^9$	$4.22 \times 10^9$	$1.10 \times 10^{10}$	$2.06 \times 10^{10}$	0.083	0.161	0.258	0.291	0.320
COSMOS30679	$9.42 \times 10^8$	$1.65 \times 10^9$	$1.20 \times 10^{10}$	$2.65 \times 10^{10}$	0.718	0.831	0.906	0.991	1.141
CDFS3865	$6.31 \times 10^9$	$6.52 \times 10^9$	$1.43 \times 10^{10}$	$1.63 \times 10^{10}$	0.184	0.196	0.211	0.230	0.259
CDFS6482	$1.97 \times 10^9$	$9.10 \times 10^9$	$3.27 \times 10^{10}$	$3.52 \times 10^{10}$	0.097	0.235	0.299	0.332	0.358
LAE-COSMOS-47	$5.77 \times 10^7$	$5.77 \times 10^8$	$2.13 \times 10^9$	$3.325 \times 10^9$	0	0	0	0.093	0.172

**Notes.** For each galaxy studied, we present the range of acceptable stellar masses (Columns 2–5) and dust extinctions (Columns 6–9). The ranges are determined by optimizing the fit for minimum or maximum mass or extinction with the constraint that  $\chi^2 - \chi^2(\text{best fit}) \leq 1$  (for “1 $\sigma$ ” columns) or  $\leq 4$  (for “2 $\sigma$ ” columns). All masses are in  $M_{\odot}$  units; all extinctions are rest-frame  $B$ -band.

The  $\text{H}\alpha$  line fluxes (Song et al. 2013) yield SFRs of  $17 M_{\odot} \text{yr}^{-1}$  and  $20 M_{\odot} \text{yr}^{-1}$ , respectively, before dust corrections (and  $17 M_{\odot} \text{yr}^{-1}$  and  $25 M_{\odot} \text{yr}^{-1}$  after dust corrections). This is based on the conversion  $\text{SFR}_{\text{H}\alpha} = 4.6 \times 10^{-42} (L_{\text{H}\alpha} / \text{erg s}^{-1}) M_{\odot} \text{yr}^{-1}$ , which is appropriate for a Chabrier (2003) initial mass function (IMF; Twite et al. 2012). The inferred  $\text{SFR}_{\text{H}\alpha}$  would be  $1.06 \times$  larger for a Kroupa (2001) IMF and  $1.7 \times$  larger for the IMF assumed in Kennicutt (1998). (We chose the Chabrier IMF in order to compare our results with those of Daddi et al. 2010; see Section 6 below). We correct these SFRs for dust extinction within the emitting galaxy. The uncertainty in the SFR is dominated by the uncertainty in this dust correction, which we estimate by considering the full range of extinction among models with  $\chi^2 \leq \chi_{\text{min}}^2 + 1$ , and further allowing the possibility that the extinction of  $\text{H}\alpha$  could exceed the extinction of the continuum starlight by up to a factor of two.

### 2.3. Subaru Narrowband Survey Objects

Third, we use four Ly $\alpha$  galaxies from a narrowband survey described by Hashimoto et al. (2012) and Nakajima et al. (2012). These objects are drawn from two fields—COSMOS (objects COSMOS13636 and COSMOS30679) and the Chandra Deep Field South (CDFS; objects CDFS3865 and CDFS6482). We obtained line widths for all sources by measuring the plotted FWHM of emission-line profiles in Figures 1, 2, and 5 of

Hashimoto et al. (2012). In general, the lines in this sample appear marginally resolved. In our analysis, we regard the line width measurements as upper limits, where appropriate.

The COSMOS field spectra were from Keck + NIRSPEC spectroscopy. Here, we obtained directly measured FWHMs of 16.6 and 16.5  $\text{\AA}$  for COSMOS13636 and COSMOS30679, respectively. With a resolving power of  $R = 1500$ , the instrumental resolution corresponds to 13.8  $\text{\AA}$ , which we subtract in quadrature to yield nominal velocity dispersions of  $\sigma_{\text{los}} = 57 \text{ km s}^{-1}$  and  $\sigma_{\text{los}} = 55 \text{ km s}^{-1}$ , respectively. In each case, the measurement remains consistent with a fairly broad range,  $0 < \sigma_{\text{los}} \lesssim 96 \text{ km s}^{-1}$ .

For these COSMOS field sources, we base the half-light radii on the COSMOS ACS  $i$ -band catalog, obtaining 0.79 kpc and 1.83 kpc, respectively. Finally, their SFRs as inferred from their  $\text{H}\alpha$  fluxes are  $4.4 M_{\odot} \text{yr}^{-1}$  and  $5.3 M_{\odot} \text{yr}^{-1}$  before dust correction, which become 7.4 and  $31 M_{\odot} \text{yr}^{-1}$  after correcting for our best-fitting extinction.

The CDFS field source spectra (Hashimoto et al. 2012) were obtained with Magellan + MMIRS and have a somewhat lower resolving power ( $R \approx 1120$ , corresponding to 18  $\text{\AA}$  for  $\text{H}\alpha$ ). The measured FWHMs are 23  $\text{\AA}$  for CDFS3865 and 20  $\text{\AA}$  for CDFS6482. Subtracting the instrumental resolution in quadrature yields velocity dispersions of 105  $\text{km s}^{-1}$  and 42  $\text{km s}^{-1}$ , respectively, where again there is considerable uncertainty for the narrower, semi-resolved line (consistent with

$0 < \sigma < 70 \text{ km s}^{-1}$ ). The SFRs for these sources, based on their  $\text{H}\alpha$  line fluxes, are  $64 M_{\odot} \text{ yr}^{-1}$  and  $16 M_{\odot} \text{ yr}^{-1}$  prior to dust correction and  $96 M_{\odot} \text{ yr}^{-1}$  and  $29 M_{\odot} \text{ yr}^{-1}$  afterward.

For the physical sizes of the CDFS sources, we down-loaded archival *HST* imaging from the GEMS survey (Rix et al. 2004) and measured the half-light radii. We used the SExtractor (Bertin & Arnouts 1996) half-light radius and, as a consistency check, we also measured the fluxes in a series of circular apertures and interpolated the resulting photometric growth curve. Both methods gave consistent answers, with half-light radii of 0.96 kpc for CDFS3865 and 1.78 kpc for CDFS6482.

#### 2.4. ESO $z = 2.25$ Survey Object

Finally, we use one  $\text{Ly}\alpha$  galaxy, LAE-COSMOS-47, from a narrowband-selected  $z = 2.25$  COSMOS field sample obtained by Nilsson et al. (2011) using the ESO 2.2 m telescope, with follow-up observations obtained by Fynbo and collaborators using the X-Shooter spectrograph (Vernet et al. 2011) on the Very Large Telescope. The X-Shooter spectrum revealed  $\text{FWHM}(\text{H}\alpha) = 6.4 \pm 2 \text{ \AA}$  and  $\text{FWHM}(\text{O III}) = 4.65 \pm 0.8 \text{ \AA}$ . After correcting for instrumental resolution (with a resolving power  $R \approx 5200$ ), the  $[\text{O III}]$  line gives  $\sigma_{\text{los}} = 27_{-9}^{+8} \text{ km s}^{-1}$  and the  $\text{H}\alpha$  line gives  $\sigma_{\text{los}} = 29_{-20}^{+14} \text{ km s}^{-1}$ . The weighted average is  $\sigma_{\text{los}} = 27_{-8}^{+7} \text{ km s}^{-1}$ . The SFR, derived from the  $\text{H}\alpha$  line flux, is  $16 M_{\odot} \text{ yr}^{-1}$ . The half-light radius, from the COSMOS ACS catalog (Leauthaud et al. 2007), is 1.14 kpc.

### 3. DYNAMICAL MASS ESTIMATES

The measured velocity dispersions  $\sigma$  from the rest-frame optical emission lines are a good estimate of the total luminosity-weighted kinematics of the gas. The galaxies we are studying are spatially unresolved even in  $\sim 0.5$  seeing, meaning that the ground-based spectra we use effectively sample the integrated light, with no important dependence on slit width.

The precise conversion from velocity width to mass will depend on the kinematic structure of these galaxies. For a pure rotation-supported disk model with a flat rotation curve, we expect a line-of-sight velocity width

$$\sigma_{\text{los}}^2 = \sin^2 i v_c^2 / 2. \quad (1)$$

(Here, we assume that all particles follow circular orbits, with independent orbital phases, but with the same speed  $v_c$  and inclination angle  $i$ , where  $i = 90^\circ$  corresponds to an edge-on system. The factor of 1/2 comes from averaging over an azimuthal angle  $\phi$ :  $\langle \sin^2(\phi) \rangle = 1/2$ .)

We obtain the simplest dynamical mass estimate from these measurements by calculating the gravitating mass needed to hold the outermost particles in a galaxy (at some radius  $r_{\text{max}}$ ) in circular motion. This gives  $GM(< r_{\text{max}}) r_{\text{max}}^{-2} = v_c^2 r_{\text{max}}^{-1}$ . Solving for mass,

$$M_{\text{dyn}} \geq v_c^2 r_{\text{max}} / G, \quad (2)$$

where  $M_{\text{dyn}}$  is a lower bound because it cannot account for mass located beyond  $r_{\text{max}}$ . Measuring  $r_{\text{max}}$  is problematic. We can estimate  $r_{\text{max}}$  as the largest radius where light is observed, but it then becomes sensitive to the depth of the imaging data.

A more practical choice of radius is the effective radius  $r_e$ , defined as the radius that encloses half of the galaxy's light in projection. If we presume that the half-light radius is also the

half-mass radius, our revised estimate of the dynamical mass becomes

$$M_{\text{dyn}} \approx 2 v_c(r_e)^2 r_e / G \approx 4 \sigma_{\text{los}}^2 r_e / (G \sin^2 i) \gtrsim 4 \sigma_{\text{los}}^2 r_e / G. \quad (3)$$

The resulting mass estimates range from  $10^9$  to  $10^{10} M_{\odot}$  and are summarized in Table 2. We also tabulate their associated statistical uncertainties, which we estimate using the random errors both in  $\sigma_{\text{los}}$  and  $r_e$ . The  $\sigma_{\text{los}}$  uncertainties are estimated by adding simulated noise to spectra and re-measuring the line widths. The  $r_e$  uncertainties are in the 5%–15% range for our sample, following the treatment of Venemans et al. (2005), who use  $\delta r_e \approx r_e / (s/n)$ . The  $\sigma_{\text{los}}$  uncertainties dominate the random errors in  $M_{\text{dyn}}$ .

Several circumstances could affect our estimated masses. A rotating disk with  $i < 90^\circ$  would reduce the measured  $\sigma_{\text{los}}$  (relative to the edge-on case). Also, in our spatially unresolved spectroscopy, the observed  $\sigma_{\text{los}}^2$  reflects the luminosity-weighted average kinematics. If a significant fraction of the galaxy's light is emitted from regions where the local circular speed  $v_c(r)$  is below the maximum circular speed ( $v_{\text{max}}$ ), we should expect the weighted average  $\sigma_{\text{los}}^2$  to underestimate  $v_{\text{max}}$  and hence the mass. The precise magnitude of this effect depends on the galaxy's light profile and rotation curve. Also, like any dynamical mass based on luminous tracers, our estimate is insensitive to mass located outside the luminous matter distribution of the galaxies. If the galaxies are embedded in extended dark matter halos, the total mass of the halo could be many times the mass estimates derived from the observed  $r_e$  and  $\sigma_{\text{los}}^2$ .

Turbulence in the galaxy's gas would contribute to the measured  $\sigma_{\text{los}}$ , although in virial equilibrium that turbulence would constitute a source of pressure support and the ordered rotation of the galaxy would be correspondingly reduced. Most interestingly, if the galaxy is not in equilibrium at all, our assumed relations between kinematics and mass could be substantially wrong. Our mass estimate implicitly assumes that the virial theorem is fulfilled, that is, that the kinetic energy  $K$  and potential energy  $U$  of the galaxy are related by  $K = -U/2$ . On the other hand, in a cold accretion scenario, new material falling into a galaxy for the first time should have  $K = -U$ , i.e., the motions are faster for the same gravitating mass under these conditions and the mass inferred from gas motions would be correspondingly overestimated by a factor up to  $\sim 2$ .

Given these uncertainties, it is best to regard our direct dynamical mass estimates as approximate numbers, good to a factor of perhaps two when regarded as lower bounds on the true dynamical mass. Other dynamical mass estimates in the literature consider a more general scaling coefficient so that  $M_{\text{dyn}} = \beta \sigma_{\text{los}}^2 r_e / G$  (see Toft et al. 2012 and references therein, especially Jorgensen et al. 1996 and Cappellari et al. 2006). These works favor  $\beta \approx 5$  for early-type galaxies with Sersic indices  $n \approx 4$  and find that despite theoretical expectations for some increase of  $\beta$  with decreasing Sersic  $n$ , the observational evidence favors  $\beta \approx 5$  for a wide range of  $n$ . Thus, the simple arguments that led us to use  $\beta = 4$  come fairly close to the correct dynamical masses.

A complementary approach to interpreting the kinematic data of these galaxies is to use their linewidths to place them on some form of the Tully–Fisher relation and so to compare them on an equal footing with other galaxy populations. Such an approach avoids the difficulties associated with identifying the right radius to use in estimators of the form  $M \sim v^2 R / G$ . For high-redshift galaxy populations, a small scatter with weak redshift evolution has been demonstrated for the SMTF relation, and we place our

galaxies on such a relation in Section 5 below. To do so, we first need their stellar masses.

#### 4. POPULATION SYNTHESIS MODELING

All of the galaxies we study have extensive multiband photometry in the literature, generally including multiband optical data, some deep ground-based, near-infrared photometry, and *Spitzer* IRAC (Fazio et al. 2004) observations that are deep enough to be constraining in at least the  $3.6\ \mu\text{m}$  channel.

We have used these data to derive stellar mass estimates for the full sample. Stellar mass estimates are also available in the published literature for many of these galaxies (Finkelstein et al. 2011; Hashimoto et al. 2012; Nakajima et al. 2012; McLinden et al. 2013). While these values are mostly consistent with our estimates where samples overlap, we opted to fit the entire sample using a single procedure to avoid potential difficulties comparing masses derived using different methodologies.

##### 4.1. General Comments on SED Fitting

(1) The strong Ly $\alpha$  emission in these objects requires the presence of a young stellar population, whose ultraviolet light ionizes interstellar hydrogen that then recombines to produce the observed Ly $\alpha$  radiation. (2) The amount of dust in the fitting is essentially determined by the UV spectral slope (cf. Meurer et al. 1997; Hathi et al. 2008; Finkelstein et al. 2011). (3) In some objects, no stars older than  $10^7$  yr are *required* to explain the observed light. (4) A considerable mass in old stars is *permitted*. (5) The ionizing photon production for the best-fit stellar populations can be converted to a Ly $\alpha$  luminosity by assuming that two-thirds of the ionizing photons are ultimately converted to Ly $\alpha$  radiation (as expected under Case B recombination with a negligible escape fraction for ionizing photons). Combining this line luminosity estimate with the directly measured Ly $\alpha$  line flux gives an estimate of the escape fraction for the Ly $\alpha$  photons. These escape fractions are sensitive to the details of the star formation history over the last  $\sim 6$  Myr. We can say with reasonable confidence that the resulting escape fraction is of the order of half for the most plausible models and that Ly $\alpha$  escape fractions below 20%–30% are ruled out unless we change the stellar population in some way that dramatically increases the ionizing photon production. (6) The estimated stellar population ages and masses would increase dramatically if we did not account for the [O III] $\lambda\lambda 4959, 5007$  line fluxes. In this case, the stellar population fitting code attempts to interpret the red  $H - K$  color and the bright flux in the rest-frame 5000 Å range as due to older stellar populations. This effect can exceed an order of magnitude in both age and mass when the filter containing the [O III] $\lambda\lambda 4959, 5007$  lines is the reddest filter considered, while it is usually smaller when an additional filter redward of the 4000 Å break is included (meaning, in our case, the IRAC photometry).

##### 4.2. Starburst99 Modeling

We measured stellar masses for our sample using the Starburst99 population synthesis code (Leitherer et al. 1999). For each galaxy, we started with publicly available broadband photometry. For the seven objects in the COSMOS field, we used broadband photometry taken by the COSMOS team (Capak et al. 2007; McCracken et al. 2010), either directly from the COSMOS archive or as quoted in the papers defining the samples (Finkelstein et al. 2011; Hashimoto et al. 2012; Nakajima et al. 2012). For the two CDFS objects, we used

MUSYC survey photometry (Gawiser et al. 2006; again as quoted in Hashimoto et al. 2012 and Nakajima et al. 2012). In all cases, our final model fitting used at least nine photometric bands spanning at least the wavelength range  $0.4\ \mu\text{m} < \lambda < 3.6\ \mu\text{m}$ .

To interpret the photometry in terms of stellar population parameters, we first ran Starburst99 to generate a grid of model spectra for stellar populations at a range of ages, from  $2 \times 10^6$  yr (which is so young that no star has yet left the main sequence) up to  $2 \times 10^9$  yr (which is the age of the universe at  $z \approx 3.1$ ). We then assumed a star formation history (as described below) and generated a model spectrum by a linear combination of the spectra for particular age steps from the Starburst99 output.

We used the default Kroupa (2001) IMF in Starburst99. This is very similar to the Chabrier (2003) IMF we use elsewhere. To ensure full consistency, we adjust all quoted SFRs and stellar masses from our SED fitting by a factor of 0.94. We derived this correction factor by integrating the mass in both IMFs and assuming that the observed light is wholly dominated by stars with  $M > 1 M_{\odot}$ . This approximation is very good for  $z > 2$ , where no star with mass  $M < 1.6 M_{\odot}$  has yet left the main sequence.

We account for the mean opacity of the intergalactic medium (IGM) using the prescription of Madau (1995). We do not treat the variance in the IGM opacity in the present work. (Doing so would effectively add uncertainty to the expected fluxes in the  $u^*$ -,  $B_j$ -, and  $g$ -bands and so would improve the model  $\chi^2$ , but would not likely change the best-fit model parameters much.)

We model dust in our sample galaxies using the Small Magellanic Cloud (SMC) extinction law from Pei (1992), treating the extinction as a thin screen. The SMC law is a reasonable choice since its metallicity corresponds approximately to the few metallicity constraints so far available for Ly $\alpha$  emitters (Finkelstein et al. 2011).

We next added the directly measured spectroscopic line fluxes to the model spectrum at the appropriate wavelengths, since these emission lines are not included in the model output. This step follows the application of IGM and dust opacity, since nature has already applied these effects to the observed line fluxes.

At this point, we have a full model spectrum accounting for stellar populations, emission lines, dust, and intergalactic hydrogen absorption. We multiply this spectrum by the bandpass of each filter in the photometric data set, integrate, and normalize appropriately to obtain model fluxes in each observed filter for the model under consideration. These can be compared with the observed data to obtain the goodness-of-fit parameter  $\chi^2 = \sum_{j=1}^N (f_{j,\text{obs}} - f_{j,\text{mod}})^2 / (\delta f_{j,\text{obs}})^2$ .

To optimize the model, we fit the observed SED of the sample galaxies with a simple Monte Carlo approach that randomly varies the amount of dust and the mass in stars in each of 13 logarithmically spaced age bins and accepts a change to the model parameters using  $\chi^2$  minimization. This approach allows a more general star formation history than a single burst or an exponentially decaying SFR. While the resulting sampling of stellar ages is somewhat coarse compared with a typical single burst model, the associated uncertainty is not a dominant factor in our stellar mass estimates. The model fits usually converge to a case where 1 to 3 of the 13 mass bins dominate the luminosity at all observed wavebands. We therefore “trim” the parameter list by fixing the stellar mass to zero in bins that are clearly of minor importance and rerun the fit with only the important mass bins. This “trimming” step generally has a negligible effect on the final  $\chi^2$ , confirming that 1 to 3 simple stellar populations

can explain the observed spectrum as well as a more complex star formation history. The best-fitting model for each galaxy is presented in Table 3, where we give the ages and masses of up to three single-age stellar populations, along with the  $B$ -band dust extinction  $A_B$ , the  $\chi^2$  value of the best-fitting model, and the number of photometric points used in the SED fitting.

To further explore the parameter space of acceptable fits, we modified our code to optimize for either minima or maxima of either stellar mass or dust extinction, subject to the constraint that the model  $\chi^2$  remain close to the  $\chi^2$  of the best-fitting model for each object. We explored models with  $\Delta\chi^2 = +1$  and  $\Delta\chi^2 = +4$ . This corresponds approximately to the  $1\sigma$  and  $2\sigma$  error regions in the parameter space. The results of this exploration are summarized in Table 4, which gives the  $\pm 1\sigma$  and  $\pm 2\sigma$  ranges for both stellar mass and dust extinction.

## 5. THE STELLAR MASS TULLY–FISHER RELATION

The SMTF relation is a correlation between the kinematic line widths of galaxies and their stellar masses. The SMTF relation is more robust to differences in the stellar population mass-to-light ratio than the original Tully–Fisher relation (which correlates luminosity with line width; Tully & Fisher 1977). The relation is further generalized by Kassin et al. (2007), who demonstrated that replacing the circular speed  $V_c$  with the kinematic estimator  $S_{0.5} = (0.5V_{\text{rot}}^2 + \sigma^2)^{1/2}$  results in an SMTF that is both tighter and more applicable to the wide range of galaxy properties seen at high redshift. Here,  $V_{\text{rot}}$  characterizes the ordered rotation of a galaxy and  $\sigma$  is its disordered, random motions. Besides reduced scatter,  $S_{0.5}$  has an additional advantage: for spatially unresolved galaxies (like those we study here),  $S_{0.5}$  can be measured reasonably accurately regardless of whether the width is dominated by ordered rotation or random motions.

Our actual measurement is a single number, the line width, characterized by the observed line-of-sight velocity dispersion  $\sigma_{\text{los}}$ . We then use  $S_{0.5} = \sigma_{\text{los}}$  for our galaxies. Consider pure circular motion with a flat rotation curve of velocity  $V_c$ , viewed edge-on: we find  $\sigma_{\text{los}}^2 = \langle (\sin(\phi)V_c \rangle^2) = 0.5V_c^2$ , so that  $S_{0.5} = \sigma_{\text{los}}$ . If instead the motion is entirely random, with  $V_{\text{rot}} = 0$ , we again obtain  $S_{0.5} = \sigma_{\text{los}}$ . Only for ordered rotation in a face-on configuration do we expect  $\sigma_{\text{los}}$  to be a significant underestimate of  $S_{0.5}$ . While we cannot rule out this possibility with our data, it is likely that these galaxies are dynamically hot ( $\sigma/V_{\text{rot}} \ll 1$ ), since the stellar populations dominating the observed light are at most  $\sim 1$  dynamical time old.

Our results are shown in Figure 1, both for stellar masses from SED fitting and for dynamical masses from line width and spatial extent. The error bars for the stellar masses show the ranges of stellar mass permitted by models with  $\Delta\chi^2 \equiv \chi^2 - \chi_{\text{min}}^2 < 4$  and with  $\Delta\chi^2 \leq 1$ . The error bars for dynamical mass are determined by the uncertainties in  $\sigma_{\text{los}}$  and are diagonal since the  $x$ -axis of the plot is  $\sigma_{\text{los}}$ . For three objects from the Hashimoto et al. (2012) sample,  $\sigma_{\text{los}}$  and  $M_{\text{dyn}}$  are plotted as upper bounds.

Comparing our Ly $\alpha$  sample with the SMTF relation that Kassin et al. (2007) reported for  $0.1 < z < 1.2$  star-forming galaxies, we find that both the stellar masses and dynamical masses of Ly $\alpha$  emitters generally follow the established relation. Dynamical mass estimates show less scatter than stellar masses, as might be expected given the vagaries of star formation histories.

About half the galaxies are consistent with stellar masses falling a factor of two or more below their dynamical masses, when we account for the range of acceptable estimates for both. For these galaxies, it is possible that the dynamical mass within

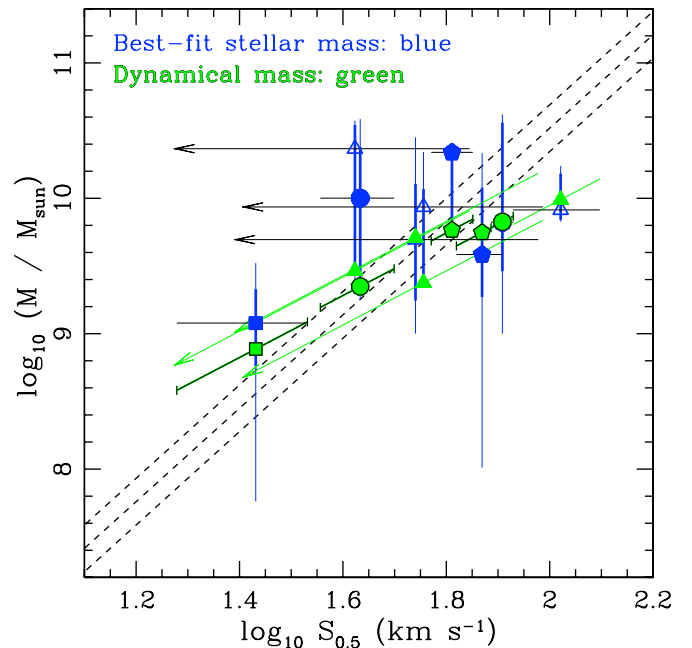


**Figure 1.** The SMTF relation and dynamical mass Tully–Fisher relation for Ly $\alpha$  emitting galaxies. For each galaxy, we plot the best-fitting stellar mass (blue) and the dynamical mass (green). The vertical bar through each pair of points spans the range of stellar masses for acceptable models (thicker line: models with  $\Delta\chi^2 < 1$ ; thinner line: models with  $1 < \Delta\chi^2 < 4$ ). The error bars on dynamical masses are diagonal, since the uncertainty in the velocity dispersion affects both plotted quantities. Dashed lines show the best-fit SMTF relation from Kassin et al. (2007) (together with its  $1\sigma$  scatter). We find that the stellar masses for Ly $\alpha$  galaxies are consistent the Kassin et al. (2007) relation, although in 3/9 cases the data also allow viable models with much lower stellar masses. Furthermore, we find that the dynamical masses of these galaxies are also consistent with the SMTF. Symbol shapes correspond to surveys: circles  $\leftrightarrow$  Bok telescope  $z = 3.1$  survey, pentagons  $\leftrightarrow$  HETDEX pilot survey, triangles  $\leftrightarrow$  Hashimoto et al. (2012) Subaru survey, and square  $\leftrightarrow$  Nilsson et al. (2011) survey. Objects with marginally resolved lines are plotted using their best-estimate values of  $\sigma$ , but can be regarded as upper limits on both  $S_{0.5}$  and  $M_{\text{dyn}}$ .

(A color version of this figure is available in the online journal.)

the central 1–2 kpc is dominated not by the young stars that power the observed Ly $\alpha$  emission, but by some other unseen component. Collisionless dark matter should not be so strongly concentrated in the central kpc of a dark matter halo. Old stars (formed from centrally concentrated gas  $\gg 10^8$  yr ago) are a possible alternative. The dynamical mass estimates we present are in fact a tighter limit on the total mass in old stars within the inner  $\sim$ kpc than the photometric limits are. Given the actively star-forming nature of these Ly $\alpha$  emitting galaxies, a reservoir of gas is the most intriguing possibility for the “excess” dynamical mass. Overall, though, such excess mass is merely permitted and not required by the data—so the Ly $\alpha$  galaxy sample shows consistency with the SMTF relation for other samples. Whatever physical properties allow Ly $\alpha$  to escape from these particular star-forming galaxies, they do not strongly affect the mass–linewidth relation.

The tight correlation observed between  $M_{\text{dyn}}$  and line width is related to the small and nearly constant physical sizes of the Ly $\alpha$  galaxy sample (Malhotra et al. 2012). A fixed physical size, combined with variable (and sometimes uncertain) line widths, can generate the observed slope of the  $M_{\text{dyn}}-S_{0.5}$  relation. The  $M_{\text{dyn}}-S_{0.5}$  relation from Kassin et al. (2007) has a somewhat steeper slope. Presuming that stars form a fairly large and constant fraction of the dynamical mass, this slope could be

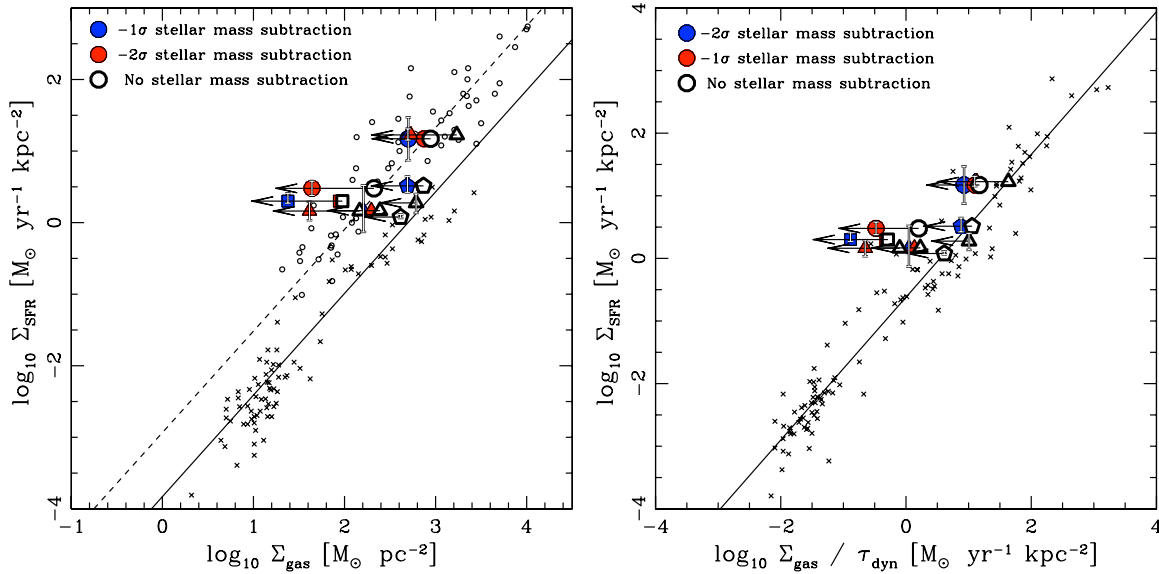


**Figure 2.** Star formation law comparison. First panel: relation between SFR surface density  $\Sigma_{\text{SFR}}$  and gas mass surface density  $\Sigma_g$ , both for our samples (large colored points) and for comparison samples drawn from Daddi et al. (2010). For each Ly $\alpha$  galaxy, the hollow point marks the upper bound on the gas surface density obtained by associating the entire dynamical mass with gas. Red and blue points take a portion of the dynamical mass to be associated with stars, using the “ $2\sigma$ ” and “ $1\sigma$ ” low-mass models from our stellar population fitting. Error bars in  $\Sigma_{\text{SFR}}$  account both for uncertainties in H $\alpha$  flux and in extinction corrections. Point styles identify subsamples, as in Figure 1. The solid line marks the relation for normal star-forming galaxies and “x” points the galaxy samples obeying that relation. The dashed line marks the starburst relation and open black circles mark the corresponding galaxies. The Ly $\alpha$  galaxies are inconsistent with the normal star formation relation and consistent with the starburst galaxy sequence. Second panel:  $\Sigma_{\text{SFR}}$  vs.  $\Sigma_g/\tau_{\text{dyn}}$ . Since Daddi et al. (2010) report a single relation here, all points from that paper have the same style. The Ly $\alpha$  galaxies are consistent with the general relation, although higher at an insignificant but intriguing level ( $\sim 2\sigma$ ).

(A color version of this figure is available in the online journal.)

interpreted as evidence for a size–linewidth relation in the Kassin et al. (2007) sample, with  $r_e \propto S_{0.5}^{\gamma}$  for  $\gamma \sim 1$ .

## 6. STAR FORMATION SCALING LAWS

We now take the dynamical mass as an upper bound on the gas mass in these galaxies and compare their properties with the scaling relations that describe star formation in other galaxy classes.

We use the gas surface mass density limit  $\Sigma_{g,\text{max}} = M_{\text{dyn}}/(2\pi r_e^2)$ . (Here, the factor of two enters because  $r_e$  is the half-mass radius and so encloses mass  $M_{\text{dyn}}/2$ .) We can improve this bound by subtracting our stellar mass estimates. In practice, our maximum stellar mass always exceeds the dynamical masses and we can subtract them to yield refined estimates of the gas mass surface density ( $\Sigma_g \lesssim (M_{\text{dyn}} - M_{\star,\text{min}})/(2\pi r_e^2)$ ).

The SFR and gas surface density can be related according to scaling laws of the form  $\log \Sigma_{\text{SFR}} \approx \alpha_{\text{SF}} \log \Sigma_g + \beta_{\text{SF}}$  (where  $\Sigma_{\text{SFR}}$  is in  $\text{M}_{\odot} \text{ yr}^{-1} \text{ kpc}^{-2}$  and  $\Sigma_g$  is in  $\text{M}_{\odot} \text{ pc}^{-2}$ ). For nearby spirals and for distant star-forming BzK galaxies, Daddi et al. (2010) find  $\alpha_{\text{SF}} = 1.42$  and  $\beta_{\text{SF}} = -9.83$  for our choice of units. For submillimeter galaxies and (U)LIRGS, Daddi et al. find a parallel but offset “starburst” sequence, with  $\beta_{\text{SF}} \approx -8.93$  (corresponding to  $8\times$  more star formation for the same gas surface density).

We determined  $\Sigma_{\text{SFR}}$  for our sample using the SFR estimates and half-light radius measurements discussed in Section 2. (In particular, we use  $\text{SFR}_{\text{H}\alpha}$  for all objects except 40844 and 27878, where  $\text{SFR}_{\text{H}\alpha}$  is unavailable, and we instead use  $\text{SFR}_{\text{sed}}$ .) We have selected a Chabrier IMF for consistency with Daddi et al. (2010). These values of  $\Sigma_{\text{SFR}}$  exceed the expectations for “normal” star-forming galaxies by a median factor of four, based

on  $\Sigma_{g,\text{max}}$  alone (i.e., assuming that all the gravitating mass is gas). The disagreement is significant at the  $>3\sigma$  level, relative to the 0.33 dex scatter in the scaling relation reported by Daddi et al. (2010). A factor of four would place the Ly $\alpha$  galaxies in between the normal and starburst sequences, although closer to the starburst sequence. If we use  $\Sigma_g = (M_{\text{dyn}} - M_{\star,\text{min}})/(2\pi r_e^2)$  in the scaling relations, we find that the median galaxy in our sample is forming stars at twice the rate expected even under the starburst scaling. The bottom line from this comparison is that Ly $\alpha$  galaxies likely belong to a family of starbursting objects that includes ULIRGS and submillimeter galaxies, despite order-of-magnitude differences in mass and SFRs.

While the “normal” and starburst galaxies follow distinct  $\Sigma_{\text{SFR}}-\sigma_g$  relations, they obey a single relation when  $\Sigma_g$  is replaced with the quantity  $\Sigma_g/\tau_{\text{dyn}}$ , where  $\tau_{\text{dyn}}$  is the dynamical time. We use  $\tau_{\text{dyn}} \approx 2\pi r_e/\sigma$  to also place our Ly $\alpha$  galaxy sample on this relation. While the Ly $\alpha$  galaxies appear less unusual when measured against this relation, they remain systematically above the trend line found by Daddi et al. (2010). The difference is suggestive, rather than significant, being a  $2\sigma$  effect. The median offset is a factor of  $\sim 3$  in  $\Sigma_{\text{SFR}}$  at fixed  $\Sigma_g/\tau_{\text{dyn}}$ . This is comparable to the 0.44 dex scatter in the relation, as reported by Daddi et al. (2010). This possible deviation should be explored using a larger sample.

The range of gas surface densities plotted in Figure 2 is from  $\sim 30$  to  $\sim 1000 \text{ M}_{\odot} \text{ pc}^{-2}$ . Based on a standard ratio of dust to gas column density,  $A_B \approx \Sigma_g/(11 \text{ M}_{\odot} \text{ pc}^{-2})$  (Bohlin et al. 1978), this corresponds to  $A_B \sim 3\text{--}90$  mag of extinction. Yet, our SED fits suggest modest extinctions,  $A_V \lesssim 1$ , in all cases. There are a few possible explanations. First, the gas surface density could be much lower than one would expect for the observed level of star formation activity. In this case, the star formation versus gas surface density scaling must be more extreme than even the starburst relation. Second, the dust-to-gas ratio could

be about 1–2 orders of magnitude lower than in the Milky Way. This would be most easily accommodated if the dust-to-gas ratio scales as the square of the metal abundance. Third, the extinctions inferred from SED fitting could be dramatic underestimates. If so, these objects’ bolometric luminosities would mostly emerge in the rest-frame far infrared, making them readily detectable with submillimeter imaging (cf. Finkelstein et al. 2009; J. L. Wardlow et al. 2013, in preparation).

## 7. DENSITIES

Given our estimates of the dynamical mass, it is straightforward to determine the mean density within the effective radius for our sample. We find

$$\bar{\rho}_e = \frac{3}{2\pi G} \frac{\sigma_{\text{los}}^2}{r_e^2} = \frac{3\pi}{Gt_{\text{orb}}^2}, \quad (4)$$

where we have used  $v_c = \sqrt{2}\sigma$  (from Equation (1), assuming  $\sin i \approx 1$ ) and  $t_{\text{orb}} = 2\pi r_e/v_c$ .

The likely descendants of high-redshift Ly $\alpha$  galaxies can be inferred by combining their observed spatial clustering (e.g., Ouchi et al. 2003; Kovač et al. 2007; Gawiser et al. 2007) with merger tree analyses. Gawiser et al. (2007) found that the typical descendants of high- $z$  Ly $\alpha$  galaxies should be  $\sim L^*$  galaxies based on their own correlation length measurement at  $z \approx 3.1$ , but could be considerably more massive ( $\sim 3\text{--}5L^*$  objects) based on the stronger correlations measured by Ouchi et al. (2003) and Kovač et al. (2007). Especially in the latter case, Ly $\alpha$  galaxy descendants should be primarily early-type systems (galaxy bulges and/or elliptical galaxies), which are the densest stellar systems in the nearby universe.

We therefore compare the density measurements for Ly $\alpha$  galaxies with the corresponding densities for early-type galaxies and bulges in Figure 3. The Ly $\alpha$  galaxy densities are the mean density within the effective radius, derived dynamically and therefore inclusive of all gravitating mass. For disk galaxy bulges, we take an intermediate-redshift sample from MacArthur et al. (2008). Here, we use the published effective radii and velocity dispersions to obtain dynamical estimates of density. We use two nearby elliptical galaxy samples (one from Kelson et al. 2000 and one compiled by Bezanson et al. 2009 from earlier work by Franx et al. 1989, Peletier et al. 1990, and Jedrzejewski 1987). For the Kelson et al. (2000) sample, we determine densities from published  $\sigma_{\text{los}}$  and  $r_e$  measurements; for the Bezanson et al. (2009) sample, we use plotted values of  $r_e$  and  $\bar{\rho}(r_e)$ . The Ly $\alpha$  galaxies are smaller at fixed density and less dense at fixed radius than the nearby ellipticals and spiral bulges. On the other hand, they tend to be smaller and denser than the handful of local ellipticals that have similar dynamical masses. We also compare with a sample of early-type galaxies at  $z \sim 2.3$  (Bezanson et al. 2009), which overlaps our Ly $\alpha$  sample in redshift. Here, the Ly $\alpha$  galaxies are of considerably lower density. In the samples from Bezanson et al. (2009), we are using *stellar* mass rather than dynamical mass, since  $\sigma_{\text{los}}$  is generally unavailable for the high-redshift early-type galaxies. Were dynamical masses available, we might expect these two samples to shift upward in Figure 3, but the effect would be modest, since the central regions of early-type galaxies are likely dominated by stellar mass.

The relation between initial overdensity and epoch of collapse ensures that bound galaxies at  $2 < z \lesssim 3$  will, by the present epoch, be parts of more massive structures. We expect that the Ly $\alpha$  galaxies we observe will grow through some combination

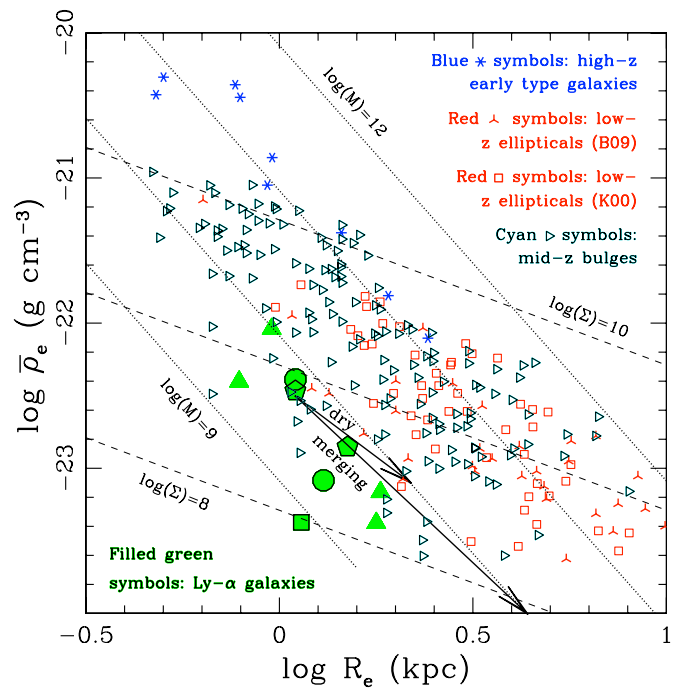


**Figure 3.** Densities and effective radii for Ly $\alpha$  galaxies (green points) and comparison samples. Cyan triangles are intermediate-redshift disk galaxy bulges from MacArthur et al. (2008) and red squares are low-redshift elliptical galaxies from Kelson et al. (2000), both with densities derived dynamically. Blue asterisks are high-redshift ( $z \sim 2.3$ ) early-type galaxies and three-pointed stars are another local early-type galaxy sample, both from Bezanson et al. (2009), and both using stellar masses estimates from SED fitting. Diagonal dotted lines mark masses of  $10^9$ ,  $10^{10}$ ,  $10^{11}$ , and  $10^{12} M_{\odot}$  and dashed lines mark surface densities of  $10^8$ ,  $10^9$ , and  $10^{10} M_{\odot} \text{ kpc}^{-2}$ . The Ly $\alpha$  galaxies are typically about  $10\times$  less massive than the local ellipticals, yet of comparable density. Non-dissipative (“dry”) merging results in galaxy densities that decrease as  $\rho \propto R_e^k$  for  $2 \leq k \leq 2.5$ , based on virial theorem arguments and conservation of total energy (see, e.g., Bezanson et al. 2009). Arrows show such scalings, with the shorter arrow corresponding to one major merger and the longer one to a mass doubling through minor mergers. Neither arrow approaches the region of the elliptical galaxy samples, indicating that dissipational merging is required if these objects are indeed progenitors of present-day, early-type galaxies.

(A color version of this figure is available in the online journal.)

of merging and smooth accretion. Merging can proceed either without dissipation, as expected for pure mergers of stellar systems (“dry mergers”), or with dissipation, as generally expected for gas-rich objects. Conservation of energy and the virial theorem can be combined to infer the expected evolution of radius with mass for dry mergers, both in the limit of equal-mass (“major”) mergers and in the limit of large mass ratio (“minor”) mergers. For major mergers, we expect  $R_e \propto M$ , while for minor mergers, we expect  $R_e \propto M^2$  (e.g., Bezanson et al. 2009). In Figure 3, these correspond to  $\rho \propto R_e^{-2}$  for major mergers and  $\rho \propto R_e^{-2.5}$  for minor mergers. We plot vectors for both scalings. These show that the Ly $\alpha$  galaxies we observe cannot grow to reproduce the observed masses, sizes, and densities of modern elliptical galaxies through simple dry merging. Instead, dissipational (“wet”) merging is required in order to grow the galaxies at an approximately constant mass density.

## 8. CONCLUSIONS

We have performed the first study of dynamical masses for high-redshift Ly $\alpha$  galaxies, using a sample of nine objects assembled from four samples (McLinden et al. 2011; Richardson

et al. 2013; Finkelstein et al. 2011; Hashimoto et al. 2012; Nakajima et al. 2012; Nilsson et al. 2011). Such studies have been previously impractical, given the small galaxy sizes that require *HST* imaging for size measurements (Malhotra et al. 2012), a faint continuum that precludes absorption line measurements, and redshifts that require near-infrared spectroscopy to access those emission lines most useful for kinematic line width measurements. We measure dynamical masses ranging from  $10^9 M_{\odot}$  to  $10^{10} M_{\odot}$ .

We combine these dynamical masses with stellar masses, to study the position of  $\text{Ly}\alpha$  galaxies on a version of the SMTF relation between mass and line width. To derive stellar masses consistently for the full sample, we fit population models to extensive multiband photometry covering rest wavelengths from  $\text{Ly}\alpha$  to beyond the 4000 Å break. This affords constraints on young stars, older stars, and dust.

We find that the  $\text{Ly}\alpha$  galaxies are broadly consistent with the SMTF relation established at lower redshift. Thus, whatever physical conditions allow the production and escape of significant  $\text{Ly}\alpha$  do not result in strong departures from the linewidth–mass relation. On the other hand, about half of the sample galaxies are consistent with stellar masses significantly below their dynamical masses. In these cases, there is a possibility of a dynamically significant reservoir of gas that is present in the inner kpc region and provides fuel for ongoing star formation. The dynamical mass measurements are in fact the most powerful constraint we have on the presence of old stars in the sample galaxies. In most cases, the stellar population fits allow up to  $\sim 3 \times 10^{10} M_{\odot}$  of old stars before the resulting light appreciably degrades the quality of the SED fit. However, dynamical constraints place a tighter limit of  $\leq 1 \times 10^{10} M_{\odot}$  on the total mass for the galaxies in our sample.

By using the dynamical masses as an upper bound on the gas mass and using the  $\text{H}\alpha$  line measurements and/or stellar population fits to infer SFRs, we have examined the way the  $\text{Ly}\alpha$  galaxies fall on the scaling relations for star formation. We conclude that they form stars more actively than the “normal” star-forming galaxy population at a comparable gas mass surface density. Their behavior is consistent with that observed in starburst galaxies, despite the typically smaller masses and sizes of the  $\text{Ly}\alpha$  galaxy population.

The dynamical masses we infer remain 1–2 orders of magnitude below the characteristic dark halo masses inferred from the clustering of  $\text{Ly}\alpha$  galaxies. Since the ratio of baryonic to dark mass should be globally uniform at around 14%, we infer that a significant part of the baryonic matter associated with these halos has not yet accreted to the central kpc, where the active star formation is observed.

Finally, we examined densities of these objects. While hierarchical structure formation models suggest that small galaxies at  $z \sim 2\text{--}3$  should become parts of early-type galaxies or spiral bulges by  $z = 0$ , the  $\text{Ly}\alpha$  galaxies are of smaller size and comparable density with present-day elliptical galaxies and of comparable size but smaller density than present-day spiral galaxy bulges. If the  $\text{Ly}\alpha$  galaxies are to evolve into either, they must do so through dissipational merging. This is consistent with the picture of  $\text{Ly}\alpha$  galaxies as young, starbursting galaxies, whose present properties and future evolution include a large role for gas physics.

We thank the DARK Cosmology Centre and Nordea Fonden in Copenhagen, Denmark, for hospitality during the completion of this work. We thank Ignacio Ferreras and Sune Toft

for helpful discussions and an anonymous referee for constructive comments. This work has been supported by the US National Science Foundation through NSF grant AST-0808165. Based in part on observations obtained at the Gemini Observatory, which is operated by the Association of Universities for Research in Astronomy, Inc., under a cooperative agreement with the NSF on behalf of the Gemini partnership: the National Science Foundation (United States), the Science and Technology Facilities Council (United Kingdom), the National Research Council (Canada), CONICYT (Chile), the Australian Research Council (Australia), Ministério da Ciência, Tecnologia e Inovação (Brazil) and Ministerio de Ciencia, Tecnología e Innovación Productiva (Argentina). This work was supported in part by a NASA Keck PI Data Award, administered by the NASA Exoplanet Science Institute. Some data presented herein were obtained at the W. M. Keck Observatory from telescope time allocated to the National Aeronautics and Space Administration through the agency’s scientific partnership with the California Institute of Technology and the University of California. The Observatory was made possible by the generous financial support of the W. M. Keck Foundation. The authors wish to recognize and acknowledge the very significant cultural role and reverence that the summit of Mauna Kea has always had within the indigenous Hawaiian community. We are most fortunate to have the opportunity to conduct observations from this mountain.

## REFERENCES

- Bertin, E., & Arnouts, S. 1996, *A&AS*, **117**, 393  
 Bezanson, R., van Dokkum, P. G., Tal, T., et al. 2009, *ApJ*, **697**, 1290  
 Bohlin, R. C., Savage, B. D., & Drake, J. F. 1978, *ApJ*, **224**, 132  
 Bond, N. A., Gawiser, E., Gronwall, C., et al. 2009, *ApJ*, **705**, 639  
 Capak, P., Aussel, H., Ajiki, M., et al. 2007, *ApJS*, **172**, 99  
 Cappellari, M., Bacon, R., Bureau, M., et al. 2006, *MNRAS*, **366**, 1126  
 Chabrier, G. 2003, *PASP*, **115**, 763  
 Daddi, E., Elbaz, D., Walter, F., et al. 2010, *ApJL*, **714**, L118  
 Fazio, G. G., Hora, J. L., Allen, L. E., et al. 2004, *ApJS*, **154**, 10  
 Finkelstein, S. L., Hill, G. J., Gebhardt, K., et al. 2011, *ApJ*, **729**, 140  
 Finkelstein, S. L., Malhotra, S., Rhoads, J. E., Hathi, N. P., & Pirzkal, N. 2009, *MNRAS*, **393**, 1174  
 Finkelstein, S. L., Rhoads, J. E., Malhotra, S., Pirzkal, N., & Wang, J. 2007, *ApJ*, **660**, 1023  
 Franx, M., Illingworth, G., & Heckman, T. 1989, *AJ*, **98**, 538  
 Gawiser, E., Francke, H., Lai, K., et al. 2007, *ApJ*, **671**, 278  
 Gawiser, E., van Dokkum, P. G., Herrera, D., et al. 2006, *ApJS*, **162**, 1  
 Guaita, L., Gawiser, E., Padilla, N., et al. 2010, *ApJ*, **714**, 255  
 Hashimoto, T., Ouchi, M., Shimasaku, K., et al. 2013, *ApJ*, **765**, 70  
 Hathi, N. P., Malhotra, S., & Rhoads, J. E. 2008, *ApJ*, **673**, 686  
 Jedrzejewski, R. I. 1987, *MNRAS*, **226**, 747  
 Jorgensen, I., Franx, M., & Kjaergaard, P. 1996, *MNRAS*, **280**, 167  
 Kassin, S. A., Weiner, B. J., Faber, S. M., et al. 2007, *ApJL*, **660**, L35  
 Kelson, D. D., Illingworth, G. D., van Dokkum, P. G., & Franx, M. 2000, *ApJ*, **531**, 184  
 Kennicutt, R. C., Jr. 1998, *ARA&A*, **36**, 189  
 Kovač, K., Somerville, R. S., Rhoads, J. E., Malhotra, S., & Wang, J. 2007, *ApJ*, **668**, 15  
 Kroupa, P. 2001, *MNRAS*, **322**, 231  
 Leauthaud, A., Massey, R., Kneib, J.-P., et al. 2007, *ApJS*, **172**, 219  
 Leitherer, C., Schaerer, D., Goldader, J. D., et al. 1999, *ApJS*, **123**, 3  
 MacArthur, L. A., Ellis, R. S., Treu, T., et al. 2008, *ApJ*, **680**, 70  
 Madau, P. 1995, *ApJ*, **441**, 18  
 Malhotra, S., Rhoads, J. E., Finkelstein, S. L., et al. 2012, *ApJL*, **750**, L36  
 McCracken, H. J., Capak, P., Salvato, M., et al. 2010, *ApJ*, **708**, 202  
 McLinden, E. M., Finkelstein, S. L., Rhoads, J. E., et al. 2011, *ApJ*, **730**, 136  
 McLinden, E. M., Rhoads, J. E., Malhotra, S., et al. 2013, *MNRAS*, submitted  
 Meurer, G. R., Heckman, T. M., Lehnert, M. D., Leitherer, C., & Lowenthal, J. 1997, *AJ*, **114**, 54  
 Nakajima, K., Ouchi, M., Shimasaku, K., et al. 2013, *ApJ*, **769**, 3  
 Nilsson, K. K., Östlin, G., Møller, P., et al. 2011, *A&A*, **529**, 9

- Ouchi, M., Shimasaku, K., Furusawa, H., et al. 2003, *ApJ*, **582**, 60
- Partridge, R. B., & Peebles, P. J. E. 1967, *ApJ*, **147**, 868
- Pei, Y. C. 1992, *ApJ*, **395**, 130
- Peletier, R. F., Davies, R. L., Illingworth, G. D., Davis, L. E., & Cawson, M. 1990, *AJ*, **100**, 1091
- Pirzkal, N., Malhotra, S., Rhoads, J. E., & Xu, C. 2007, *ApJ*, **667**, 49
- Richardson, M. L. A., Levesque, E. M., McLinden, E. M., et al. 2013, *AJ*, submitted
- Rix, H.-W., Barden, M., Beckwith, S. V. W., et al. 2004, *ApJS*, **152**, 163
- Song, M., Finkelstein, S. L., Gebhardt, K., et al. 2013, *ApJ*, submitted
- Toft, S., Gallazzi, A., Zirm, A., et al. 2012, *ApJ*, **754**, 3
- Tully, R. B., & Fisher, J. R. 1977, *A&A*, **54**, 661
- Twite, J. W., Conselice, C. J., Buitrago, F., et al. 2012, *MNRAS*, **420**, 1061
- Venemans, B. P., Röttgering, H. J. A., Miley, G. K., et al. 2005, *A&A*, **431**, 793
- Vernet, J., Dekker, H., D'Odorico, S., et al. 2011, *A&A*, **536**, A105